M-center in 4H-SiC: Isothermal DLTS and first principles modeling studies

View Online   Export Citation   CrossMark

I. Capan,[1,a] T. Brodar,[1] R. Bernat,[1] Ž. Pastuović,[2] T. Makino,[3] T. Ohshima,[3] J. D. Gouveia,[4] and J. Coutinho[4]

AFFILIATIONS

[1]Rudjer Bošković Institute, Bijenička 54, 10000 Zagreb, Croatia

[2]Australian Nuclear Science and Technology Organisation, 1 New Illawarra Rd., Lucas Heights, NSW 2234, Australia

[3]National Institutes for Quantum and Radiological Science and Technology, 1233 Watanuki, Takasaki, Gunma 370-1292, Japan

[4]I3N, Department of Physics, University of Aveiro, Campus Santiago, 3810-193 Aveiro, Portugal

Note: This paper is part of the Special Topic on Defects in Semiconductors.
[a]**Author to whom correspondence should be addressed:** ivana.capan@irb.hr

ABSTRACT

We report on a bistable defect known as M-center, here introduced in n-type 4H-SiC by 2 MeV He ion implantation. Deep levels of the M-center are investigated by means of junction spectroscopy techniques, namely, deep level transient spectroscopy (DLTS) and isothermal DLTS. In addition to previously reported three deep levels arising from the M-center (labeled as M_1, M_2, and M_3), we provide direct evidence on the existence of a fourth transition (labeled as M_4) with an activation energy of 0.86 eV. Activation energies and apparent capture cross sections for all four metastable defects are determined. From first-principles calculations, it is shown that the observed features of the M-center, including the charge state character, transition levels, bi-stability dynamics, and annealing, are all accounted for by a carbon self-interstitial.

I. INTRODUCTION

Silicon carbide, especially its 4H polytype (4H-SiC), is a mainstream material for the industry of high-power electronics.[1,2] Additionally, its wide bandgap, radiation hardness, and high breakdown field make 4H-SiC an attractive semiconductor for the fabrication of radiation detectors capable of operating under harsh environments.[3–5] Also promising is the use of SiC in quantum technologies, hosting defects capable of storing quantum bits, emitting single-photons, or working as quantum sensors.[6–9]

Intrinsic defects are of utmost relevance in the above context. Along with the vacancies, self-interstitials play a fundamental role in defect annealing, mass transport, and countless solid-state reactions, including doping activation. Hence, a detailed characterization of intrinsic defects in SiC is highly desirable and that includes their response to thermal treatments, electromagnetic fields, and traveling carriers.

Both Si and C vacancies in 4H-SiC have spectroscopic fingerprints along with consistent physical models detailing their atomistic, electronic, and vibrational structures. This knowledge has been achieved by combining experimental techniques, such as electron paramagnetic resonance (EPR),[10,11] deep level transient spectroscopy (DLTS),[10,12–15] and photoluminescence (PL),[16,17] with numerical modeling, mostly density functional theoretical methods[18–21] In particular, the agreement between calculated hyperfine and zero-field splitting data with the measurements from magnetic resonance experiments has led to unequivocal assignments (see, for instance, Refs. 18 and 22).

On the other hand, relatively little is known regarding the properties of self-interstitials in 4H-SiC. Indirect evidence for their existence comes from oxidation/annealing studies. A significant reduction in carbon vacancies (as monitored by the intensity of the $Z_{1/2}$ DLTS peak)[12,23,24] was found upon thermal oxidation of 4H-SiC layers in the temperature range of 1150–1300 °C.[25,26] This process leads to the injection of interstitials into the semiconductor bulk, and it was interpreted as a result from the annihilation of vacancy–interstitials pairs also known as Frenkel pairs.[25,26] Assuming a typical pre-exponential factor for the diffusivity of the

injected species, a migration barrier in the range of 1.5–2 eV was estimated for the defect to be captured by the vacancies.[26]

From EPR, spectra EI1 (spin-1/2) and EI3 (spin-1) signals that appear in irradiated p-type 4H-SiC show features of interstitial-related defects. While originally assigned to a carbon vacancy-hydrogen complex,[27] EI3 was later connected to a carbon split-interstitial on the cubic site. Its low annealing temperature (200–250 °C)[27] and the calculated ^{29}Si hyperfine tensor elements supported this view.[28] Although these results were confirmed by subsequent calculations,[29,30] the theoretical hyperfine interactions involving ^{13}C ligands could not find an experimental match, and no model has been proposed for EI1.

Additional hints for self-interstitials in 4H-SiC have been reported by DLTS and related techniques. Examples of deep traps connected (or tentatively connected) to carbon self-interstitials (C_i) in 4H-SiC are $EH_{1/3}$, M and EB.[24,31–35] They are all radiation-induced point defects with low annealing temperature ($T < 370\,°C$). However, and despite having electron emission energies close to transition levels predicted by theory for C_i,[36,37] they cannot be related to the same defect.

Irradiation of n-type 4H-SiC with fast electrons at room temperature leads to a broad and complex DLTS spectrum in the temperature range of $T \sim 180$–360 K.[38] This is likely to arise from many different metastable and marginally stable radiation-induced defects. A gentle annealing ($T > 100\,°C$) clears away much of the broadness and "noise," unveiling several peaks, most notably $Z_{1/2}$,[12,23,24] $EH_{1/3}$,[24] $EH_{4/5}$,[24] $S_{1/2}$,[39] and M.[31,32]

Among the above, $Z_{1/2}$ ($E_c - 0.64$ eV) can be found already in the as-grown material due to its exceptionally low formation energy.[40] Irradiation simply increases its intensity. In a conventional DLTS spectrum, the signal appears as a superimposition of two (=/0) electron emissions, assigned to double-negative carbon vacancies (V_C) located on h and k sites (Z_1 and Z_2, respectively) of the 4H-SiC lattice.[12–14] EH_1 and EH_3 (with transition levels at about $E_c - 0.4$ eV and $E_c - 0.7$ eV, respectively) correspond to electron emissions from two different charge states of the same complex, possibly carbon-interstitial related.[34,41] EH_4 and EH_5 traps ($E_c - 1.0$ eV and $E_c - 1.1$ eV, respectively) were recently assigned to donor transitions of carbon antisite–vacancy (CAV) pairs aligned along different crystalline directions.[42] Essentially, the CAV defect consists of an isomer of the silicon vacancy (V_{Si}),[43–45] which is actually the most stable form of V_{Si} in the p-type material.[46,47] S_1 and S_2 show almost identical activation energies to EH_1 and EH_3. Unfortunately, $S_{1/2}$ and $EH_{1/3}$ labeling has often been used interchangeably for both traps, leading to some confusion in the literature. Recently, Alfieri and Mihaila[34] investigated this issue, and from annealing experiments, they concluded that $S_{1/2}$ and $EH_{1/3}$ must be different defects. Like the $EH_{1/3}$ pair of traps, S_1 and S_2 were ascribed to electron emissions from different charge states of the same defect,[39] most probably to $(-3/-2)$ and $(-2/-1)$ transitions of the silicon vacancy.[15,48] Finally, the M-center is a bistable defect giving rise to a family of at least three electron traps, namely, M_1 ($E_c - 0.42$ eV), M2 ($E_c - 0.63$ eV), and M3 ($\sim E_c - 0.83$ eV).[31,32]

Using conventional and isothermal deep level transient spectroscopy and first-principles calculations, we recently found that the properties of M, including bistability, annealing, reconfiguration kinetics, and electronic levels, match those of the carbon

self-interstitial.[49] In this article, we further develop our findings, including the mechanisms for reconfiguration and migration, as well as present results that exclude a connection between M and Frenkel pairs.

II. METHODS

A. Junction spectroscopy

n-type Schottky barrier diodes (SBDs) were fabricated on nitrogen-doped (up to 4.5×10^{14} cm^{-3}) 4H-SiC epitaxial layers, approximately 25 μm thick. The epi-layer was grown on an 8° off-cut silicon face of a 350 μm thick 4H-SiC (0001) wafer without a buffer layer by chemical vapor deposition.[50] The Schottky barriers were formed by thermal evaporation of nickel through a metal mask with a patterned squared aperture of 1 mm edge length, while Ohmic contacts were formed on the backside of the silicon carbide substrate by nickel sintering at 950 °C in an Ar atmosphere.

The SBDs were pattern-implanted with 2 MeV He ions with fluences of 10^9 cm^{-2}. All implantations were performed through the front nickel Schottky contact, at room temperature, and zero applied bias. The pattern-implantation of ions was performed as described in a previous study[51] at the nuclear microprobe facility of the Australian Nuclear Science and Technology Organization.

The current–voltage and capacitance–voltage characteristics of SBDs were measured by Keithley 4200 SCS (Keithley Instruments, Cleveland, USA). DLTS and isothermal DLTS measurements were performed using a Boonton 7200 capacitance meter (Boonton Electronics, New Jersey, USA) and an NI PCI-6521 data acquisition device (NI, Austin, USA). Conventional DLTS measurements were carried out in the temperature range from 100 up to 450 K with the temperature ramp rate of 2 K/min. Reverse voltage, pulse voltage, and pulse width were $V_R = -4$ V, $V_P = 0$ V, and $t_P = 10$ ms, respectively.

To study metastable defects in detail, a technique called isothermal DLTS was applied. Isothermal DLTS makes it easier to study their transformation kinetics and observe their deep levels at the same temperature.[52] Temperature-dependent emission rates and recombination rates have fixed values at specific temperatures. Moreover, metastable defects can be placed in specific configurations before each isothermal DLTS measurement. At each measurement temperature, a single capacitance transient (20 min long) was measured with the sampling rate of 60 kHz and with 72×10^6 samples. The SBD temperature was kept stable during measurements (temperature change was less than 0.05 K). Three different annealing procedures were used to control the configuration of the M-center prior to measurements. We shall refer to them later in the text as procedures 1, 2, and 3.

Procedure 1 (for conventional DLTS measurements): M-center was transformed to configuration B or configuration A by annealing at 450 K (for 20 min) and cooling SBD without applying bias (0 V) or by 20 min annealing at the temperature of 340 K and cooling down SBDs with applied bias (-30 V), respectively. The same annealing procedure was used before subsequent isothermal DLTS measurements in the temperature range of 170–188 K.

Procedure 2 (for isothermal DLTS, $T < 340$ K): The second procedure was used during isothermal DLTS measurements in the temperature range from 280 up to 340 K. M-center was initially

placed in configuration B by annealing without bias at 450 K for 20 min, which was followed by cool down without bias and a 20 min long waiting period at a measurement temperature. Capacitance transient was measured after applying reverse bias (-4 V). Next, M-center was placed in configuration A by applying reverse bias (-30 V) at the temperature of 340 K (for 20 min) and cooling down the SBD under reverse bias (-30 V) to measurement temperature. Capacitance transient was measured at the reverse voltage ($V_R = -4$ V) after applying voltage pulse ($V_P = 0$ V, $t_P = 10$ ms).

Procedure 3 (for isothermal DLTS, $T > 340$ K): The third procedure was used for isothermal DLTS measurements at temperatures above 340 K. Before isothermal DLTS measurements at temperatures above 340 K, M-center was transformed to configuration B by 20 min annealing at the temperature of 450 K without applied bias, after which the SBD was cooled down to measurement temperature followed by a 20 min waiting period. Next, two subsequent isothermal DLTS measurements were carried out. The first measurement was with M-center initially in configuration B, while the second measurement was with M-center in configuration A as the reconfiguration from configuration B to configuration A occurred during the first measurement.

B. First principles calculations

Electronic structure calculations were carried out within the range-separated hybrid density functional method using the Vienna *Ab-initio* Simulation Package (VASP).[53] The electronic exchange-correlation potential was that proposed by Heyd, Scuseria, and Ernzerhof (commonly referred to as HSE06).[54,55] Core electrons were described by the projector-augmented wave method,[56,57] while valence states were expanded in plane-waves with a cut-off energy of 420 eV.

Carbon interstitial defects were introduced in 400-atom hexagonal supercells of 4H-SiC with calculated basal and axial lattice constants $a = 3.0712$ Å and $c = 10.051$ Å, respectively. Forces acting on atomic nuclei were obtained within the Hellmann–Feynman approach and the generalized gradient approximation (GGA) to the exchange correlation interactions.[58] A conjugate gradient algorithm was used to find minimum energy structures. Residual forces on nuclei were kept below 0.01 eV/Å. For structural relaxation (GGA-level), the Brillouin zone (BZ) was sampled on a Γ-centered $2 \times 2 \times 2$ set of (symmetry-folded) **k**-points. For total energy calculations (HSE06-level), the sampling was carried out at the Γ-point (for further details and testing, see Ref. 59).

The formation energy of carbon self-interstitial defects in various charge states (q) and atomistic geometries (R) were obtained as a function of Fermi energy (E_F) using the usual formalism,

$$E_f(E_F; q, R) = E_{def}(q, R) - E_{bulk} - \mu_C + q(E_v + E_F), \quad (1)$$

where E_{def} and E_{bulk} are total energies of defective and pristine supercells, respectively, whose stoichiometric and charge imbalances are accounted for by the chemical potential of the carbon species (μ_C) and that of electrons ($\mu_e = E_v + E_F$) trapped by or emitted from the C_i defect. The chemical potential of carbon is the energy per atom in crystalline diamond, thus corresponding to a carbon-

rich grown material. The electron chemical potential is the Fermi level offset by the valence band maximum energy, obtained as the highest occupied Kohn–Sham state in bulk 4H-SiC. We note that E_{def} includes a correction to the periodic effects of charged supercells.[60]

Defect transformation and migration mechanisms were investigated using the climbing image nudged elastic band method (CI-NEB).[61] We started by forming a sequence of 7–11 intermediate structures between the end-configurations. An exploratory NEB calculation was then performed using the Γ-point for sampling the BZ for a fast pre-relaxation of the minimum energy path. The image sequence was further improved by performing a subsequent NEB relaxation with a Γ-centered $2 \times 2 \times 2$ mesh for the BZ sampling. Finally, a self-consistent calculation within the HSE06-level was carried out for transition state geometry.

III. EXPERIMENTAL RESULTS

A. Deep level transient spectroscopy measurements

Figure 1 shows DLTS spectra for 4H-SiC SBDs implanted with 2 MeV He ions and measured in the above explained configurations A and B (procedure 1). In addition to $Z_{1/2}$, a well-known deep level in the 4H-SiC material, and previously assigned to a transition between double negative and neutral charge state of carbon vacancy, $V_C(=/0)$,[10] three deep levels with activation energies of 0.4, 0.7, and 0.9 eV below the conduction band minimum are observed. Two deep levels at 0.4 and 0.7 eV resemble the previously reported EH_1/EH_3 and S_1/S_2. As already explained in the text (see Introduction), the relation between EH_1/EH_3 and S_1/S_2 is far from clear. This topic deserves an independent investigation. In this article, we will refer to these deep levels as S_1 and S_2 through the text.

The broad feature known as EH_4 (Fig. 1) with an activation energy of 0.9 eV was recently connected to a superposition of ($+/0$) transitions from three (out of four) carbon antisite-carbon vacancy
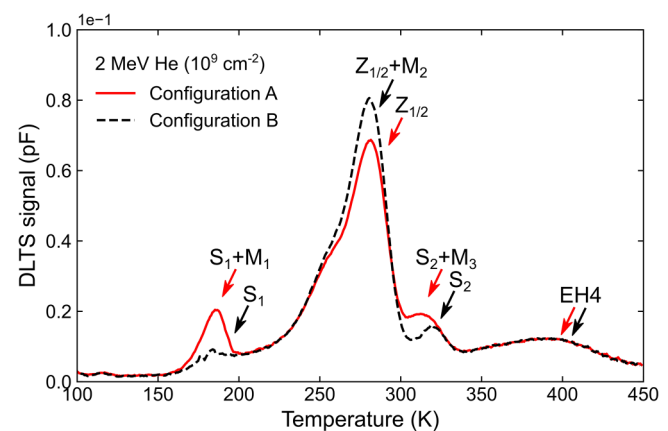

FIG. 1. DLTS spectra of 2 MeV He implanted 4H-SiC SBD in two configurations of the M-center (configuration A and configuration B).

defect orientations in the 4H-SiC lattice. The fourth orientation was assigned to a deeper EH_5 peak (see Ref. 42 for further details).

As seen in Fig. 1, the M_1 and M_3 deep levels of the M-center were observed in configuration A where they overlap with S_1 and S_2 deep levels, respectively, while the M_2 deep level was observed in configuration B where it overlaps with $Z_{1/2}$.

B. Isothermal deep level transient spectroscopy measurements

To obtain additional information about the M-center, which will enable a better understanding of this puzzling defect, we have applied the isothermal DLTS technique that is suitable for studying deep levels and reconfiguration kinetics of metastable defects. The main aim for the usage of isothermal DLTS was the search for the existence of a fourth M-peak (M_4), which was indirectly deduced by Nielsen et al.[32] (Fig. 1 of that reference). The M_4 transition is not accessible by means of conventional DLTS due to the technical limitations.

The configuration of the M-center was well defined before each measurement of the capacitance transient at specific temperature. A wide range of transient time constants ($10^{-2}-10^3$ s) was observed in the isothermal DLTS spectra. The measured time constants are linked to electron emission rates of deep levels, reconfiguration rates, or both.

Figure 2 shows the isothermal DLTS spectra measured at the temperature of M_1 and S_1 deep levels using the procedure 2. Signals of M_1 and S_1 deep levels overlap in the isothermal DLTS spectra when the M-center is in configuration A, while only S_1 deep level is observed in configuration B [Fig. 2(a)]. The signal due to the M_1 deep level (solid line) is clearly observed in the differential signal (conf. A–conf. B) of the isothermal DLTS spectra [Fig. 2(b)]. Here, the dashed curve represents the simulated isothermal DLTS signal obtained by nonlinear fitting using the following

equation:[62]

$$\text{Isothermal DLTS}(T) = C_0$$
$$+ \sum_i \frac{\Delta C_i}{\tau e_{n,i}} \exp(-\tau_d e_{n,i}) \left[1 - \exp\left(-\frac{\tau e_{n,i}}{2}\right) \right]^2, \quad (2)$$

where τ is the time constant, $e_{n,i}$ is the emission rate of transition i, ΔC_i is the amplitude of the respective capacitance transient, and C_0 is the offset. Dashed curves in Figs. 2(b) and 3(b) show results of nonlinear regression.

Figure 3 shows the isothermal DLTS spectra measured at the temperature of M_2, M_3, and M_4 deep levels using procedure 3. As already observed by conventional DLTS (Fig. 2), M_2 and M_3 overlap with $Z_{1/2}$ and S_2, respectively. An overlap of the new deep level M_4 with EH_4 is also detected. However, the M_4 peak is more clearly observed in the differential spectrum [Fig. 3(b)]. This is a direct evidence of the existence of the fourth metastable deep level, M_4, as previously postulated by Nielsen et al.[32]

C. Analysis of the M-center traps

With all four metastable deep levels being experimentally detected, we can proceed with the analysis to estimate parameters needed for the M-center identification. Activation energies for electron emission and apparent capture cross sections for M_1, M_2, M_3, and M_4 deep levels are determined from Arrhenius plots of T^2-corrected electron emission rates (Fig. 4). The activation energy and apparent capture cross section of the M_4 deep level are $E_c-0.86$ eV and 4×10^{-15} cm^2, respectively. All obtained values are listed in Table I.

The obtained activation energies for M_1 ($E_c-0.42$ eV), M_2 ($E_c-0.65$ eV), and M_3 ($E_c-0.74$ eV) are in an excellent agreement with previously reported values (0.41–0.42, 0.63–0.70, and 0.75–0.9 eV below the conduction band bottom, respectively).[31,32] As far as the apparent capture cross section is concerned, a certain
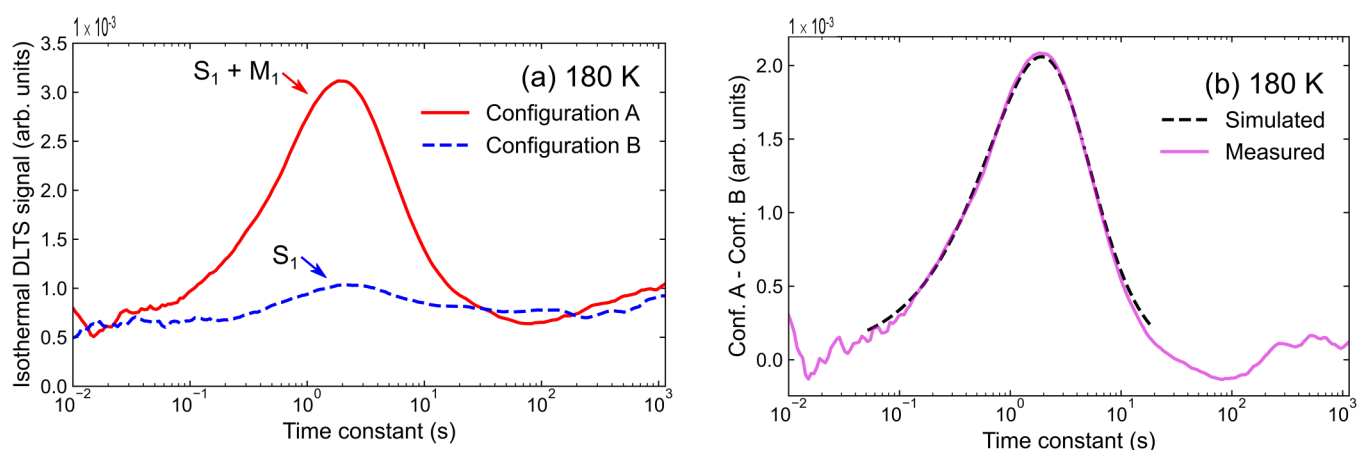

FIG. 2. (a) Isothermal DLTS spectra of the M-center in configurations A (red) and B (blue) at 180 K. M_1 overlaps with S_1. (b) Difference signal (conf. A–conf. B) of isothermal DLTS spectra shown in (a). The dashed curve represents the simulated signal obtained by nonlinear fitting.
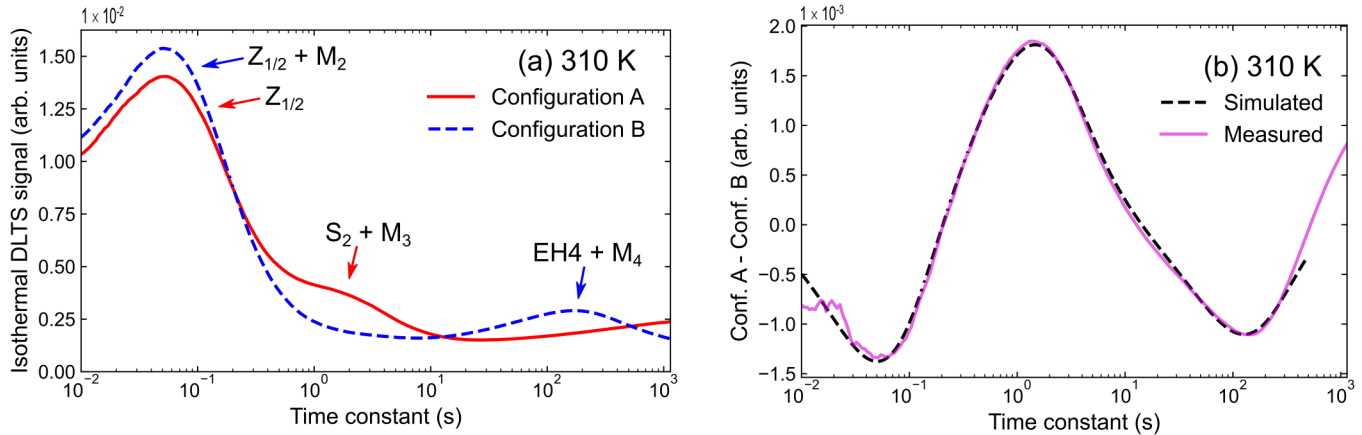
FIG. 3. Isothermal DLTS spectra of the M-center in configurations A (red) and B (blue) at 310 K. M_2, M_3, and M_4 overlap with $Z_{1/2}$, S_2, and EH_4, respectively. (b) Difference signal (conf. A–conf. B) of isothermal DLTS spectra shown in (a). The dashed curve represents the simulated signal obtained by nonlinear fitting.

discrepancy with reported values is seen. Surprisingly, all four apparent capture cross sections estimated from Arrhenius plots are of the same order of magnitude, 10^{-15} cm^2 (see Table I), indicating acceptor-like defects. However, it should be noted that this result is not well aligned with already established assignments of M1 and M2 as second acceptor transitions and M3 as the first acceptor transitions.[32] To obtain more accurate values, direct capture cross section measurements are performed, as explained later in the text.

The concentrations of M-center deep levels were determined using differential isothermal capacitance transient amplitudes [Figs. 2(b) and 3(b)] obtained by nonlinear fitting using Eq. (2) and 1 MHz C–V characteristics measured at 180 and 310 K. The Lambda effect was taken into account.[63] The obtained concentrations for all M-center deep levels are of the same order of magnitude, 10^{11} cm^{-3}.

To obtain more accurate values for the capture cross sections, we applied direct cross section measurements in the temperature ranges of 165–200 and 280–315 K. Isothermal DLTS spectra were measured subsequently with increasing pulse width from 100 ns up to 10 ms. In configuration B at temperatures above 280 K, reverse bias was applied to empty M_2 deep level before the following measurements. Measured transients were long enough (2–130 s) to observe M_2 and M_3 deep levels in the differential signal (conf. A–conf. B) of isothermal DLTS spectra and short enough to avoid significant reconfiguration of the M-center.

Figure 5 shows capture kinetics for M_1 deep level measured at 180 K and for M_2 and M_3 deep levels measured at 310 K. The model derived by Pons,[64] which considers a capture in the Debye tail, was used to describe the measured capacitance amplitudes,

$$\Delta C(t_p) = \Delta C \frac{N_T}{2N_D} R(t_p) \left[\left(1 - \frac{L_0}{W(V_R)} \right)^2 - \left(\sqrt{1 - \frac{|V_P - V_R|}{V_R + V_{Bi} - k_B T/q}} - \frac{L_1(t_p)}{W(V_R)} \right)^2 \right],$$ (3)

where V_{Bi} is the built-in potential, L_0 is the Debye length, N_T is the concentration of the M-center, N_D is the doping concentration, and W is the space charge region width. According to the model, $R(t_p)$ amplitude corresponds to the occupancy of deep levels in the depth region from $W(V_P) - L_1$ up to $W(V_R) - L_0$.

The partial transformation from configuration B to configuration A occurred during the subsequent measurements at temperatures above 280 K. Therefore, capacitance amplitudes of M_2 and M_3 deep levels in Fig. 5(b) were multiplied by the measured factors $N_T/[B]$ to rectify the effect of decreased [B] concentration of the M-center in configuration B and improve the fit. The subsequent measurements,

with pulse width 10 ms and all other settings maintained, were carried out to measure a decrease in M_2 and M_3 deep level amplitudes and determine the factor $N_T/[B]$ for each data point.

The full list of all estimated parameters is given in Table I. The capture barriers obtained by the Arrhenius plot analysis were less than 0.05 eV, while the temperature dependence of capture cross sections was not detected. The values obtained from directly measured capture cross section measurements are much better correlated with the assignments of M_3 as first acceptor transition and M_1 and M_2 as second acceptor transitions, compared to values obtained from Arrhenius plots.
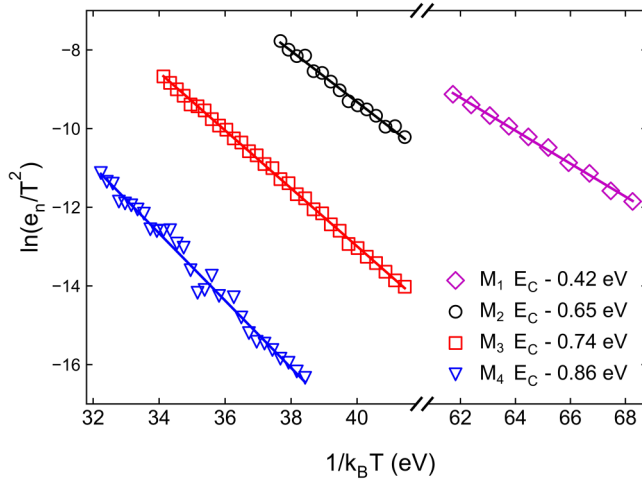
FIG. 4. Arrhenius plots of the electron emission rates for M_1, M_2, M_3, and M_4 deep levels obtained by isothermal DLTS measurements.

TABLE I. Activation energies E_a, apparent capture cross sections σ_a, directly measured capture cross section σ_d, and concentrations of the M-center deep levels determined by isothermal DLTS technique.

Deep level	E_a (eV)	σ_a (cm^2)	σ_d (cm^2)	Concentration (cm^{-3})
M_1	0.42 ± 0.01	5×10^{-15}	8×10^{-17}	8×10^{11}
M_2	0.65 ± 0.02	5×10^{-15}	5×10^{-17}	7×10^{11}
M_3	0.74 ± 0.01	4×10^{-15}	$\geq 6 \times 10^{-16}$	7×10^{11}
M_4	0.86 ± 0.02	4×10^{-15}		7×10^{11}

Additional attempts to directly measure the capture cross section for M_4 were not successful, the reason being that the M_4 emission rate is too close to reconfiguration rate from conf. B to conf. A. Therefore, the isothermal DLTS signal for M_4 cannot be subsequently measured, as needed for capture cross section measurements.

With the basic defect parameters estimated (see Table I), we now summarize all relevant transitions between different states of the M-center (Fig. 6). The states are denoted with A^q/B^q labels, which contain the corresponding configuration A or B and charge q of the M-center. Electron emission (e_n), electron capture (c_n), and reconfiguration rates (R) are indicated by arrows and respective labels.
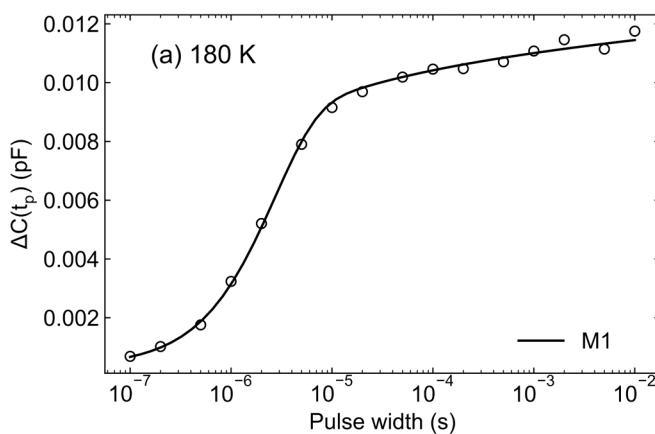
Electron emissions from the M-center, which occur after placing the M-center in the $A^=$ or $B^=$ state, result in the measured isothermal DLTS signal [Figs. 2(b) and 3(b)]. The M_4 peak in the isothermal DLTS spectra could result from electron emission $e_{n,M4}$ or the reconfiguration process in the negative charge state $R^-_{B\rightarrow A}$ followed by a faster electron emission $e_{n,M3}$. That is, the observed capacitance transient is a result of electron emission from the M-center, whether it occurs by process $B^- \rightarrow B^0 + e^-$ or $B^- \rightarrow A^- \rightarrow A^0 + e^-$. In case the reconfiguration rate in negative charge is negligible ($R^-_{B\rightarrow A} \ll e_{n,M4}$), the Arrhenius plot analysis gives the energy position of the M_4 deep level. Otherwise ($R^-_{B\rightarrow A} \gtrsim e_{n,M4}$), the M_4 deep level is not directly observed, and the measured activation energy refers to the sum of reconfiguration rate and emission rate $R^-_{B\rightarrow A} + e_{n,M4}$. If the emission rate $e_{n,M4}$ is negligible, the measured emission rate of M_4 peak corresponds to the reconfiguration rate $R^-_{B\rightarrow A}$.

IV. DEFECT MODELING

A. Defect configuration and transition levels

Considering the experimental conditions for the appearance of the M-center, two strong contenders for a defect model emerge straight away—(i) a carbon self-interstitial or (ii) a Frenkel pair.
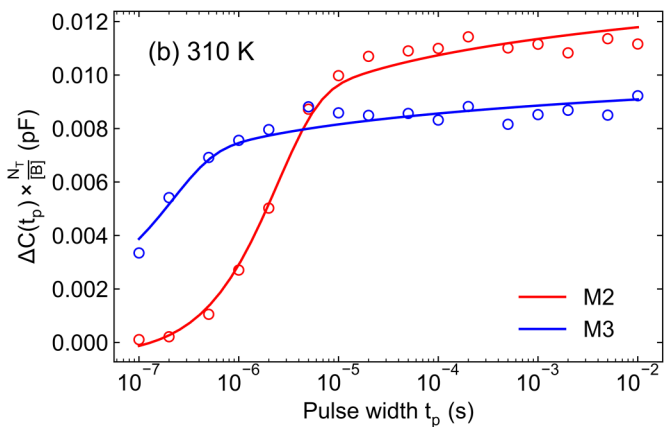

FIG. 5. Capture kinetics of M-center deep levels measured at (a) 180 and (b) 310 K. Capacitance amplitudes (data points) were determined by nonlinear fitting of the measured difference in the isothermal DLTS signal to Eq. (2). Solid lines represent the best fits of the data to Eq. (3).
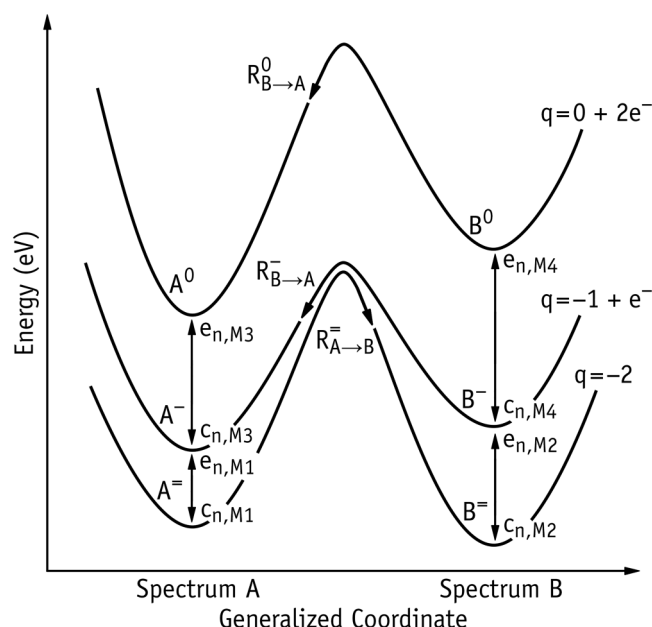
FIG. 6. Schematic configuration coordinate diagram of the M-center in 4H-SiC describing transitions (arrows) and respective rates (e_n and R) between different configurational and charge states (A^q and B^q).

We will learn that unlike the latter option, the C_i defect accounts well for the observations.

We found that all stable C_i defects in 4H-SiC comprise a C—C dimer replacing a C site. However, the local geometry depends both on its location (sub-lattice site) and the Fermi level (charge state). While in negatively charged states two Si ligands of the C_i structure are over-coordinated, neutral and positively charged states adopt a configuration analogous to the [001] split-interstitial in 3C-SiC[36,37] and diamond.[65] Among the structures with over-coordinated Si atoms, the alignment of the C—C dimer was found to be favorable either along the basal direction (henceforth labeled "b") or nearly along the main crystallographic axis (labeled "a").

Examples of the above configurations are depicted in Figs. 7(a)–7(c). They are denoted as $C_i(R)$, where the generalized coordinate R specifies the sublattice location using labels k or h, and these have subscripts a–c to identify the alignment of the dimer. Configurations involving either tetrahedral interstitial carbon atoms or Si–C split interstitials were found unstable and will not be considered hereafter.

We found that C_i can trap up to two holes or two electrons, i.e., it can form stable charge states between $q = +2$ and $q = -2$. Further carrier trapping was inspected but turned out to be energetically unfavorable. The ground state configurations are $C_i^{+2}(k_c)$, $C_i^{+1}(h_c)$, $C_i^0(h_c)$, $C_i^{-1}(h_b)$, and $C_i^{-2}(k_a)$, the neutral state adopting a spin-1 electronic configuration (like the interstitial in diamond[65] and 3C-SiC).[36,37] Structures located at the alternative sub-lattice site, $C_i^{+2}(h_c)$, $C_i^{+1}(k_c)$, $C_i^0(k_c)$, $C_i^{-1}(k_a)$, and $C_i^{-2}(h_b)$, correspond to the most favorable metastable structures. Their energies, relative to the ground state, are 0.11, 0.10, 0.21, 0.05, and 0.14 eV, respectively. We note that while C_i structures on different sub-lattice locations are separated by a large ($\gtrsim 1$ eV) barrier, the C—C dimer can reorient more easily (conserving the site, charge, and spin) by surmounting a barrier of about 0.1–0.8 eV.[49]

Using Eq. (1), we were able to construct the formation energy diagram as shown in Fig. 7(d). At this point, two important features of Fig. 7(d) are worth of mention. First, the calculated transition levels (involving transitions between states with the same sub-lattice site) in the upper half of the gap resemble those of the M-center. Calculated $(=/-)$ and $(-/0)$ transitions for $C_i(h)$ are estimated at $E_c - 0.40$ eV and $E_c - 0.76$ eV (blue line). Analogous $(=/-)$ and $(-/0)$ transitions for $C_i(k)$ are found at $E_c - 0.59$ eV and $E_c - 0.92$ eV (red line). The connection with the corresponding M-center transitions is made with the help of M_1–M_4 labels in the figure. Accordingly, M_1 and M_3 are assigned to $C_i(h)$, while M_2 and M_4 are assigned to $C_i(k)$.

The second feature relates to the bistability of the C_i defect. In a diode made of low resistivity n-type 4H-SiC, at zero bias, the Fermi level is close to the conduction band bottom and the defect finds its lowest energy state at the k-site, more precisely $C_i^{-2}(k_a)$. According to the above, this configuration gives rise to M_2 and M_4 emissions in DLTS. Conversely, under reverse bias, within the depletion region, the Fermi level is brought toward the middle of the gap, and the most stable state becomes the neutral one at the h-site, i.e., $C_i^0(h_c)$, and the defect gives rise to M_1 and M_3 emissions.

An alternative model for the M-center is a Frenkel pair (FP). Let us first consider the case of a vacancy remotely separated from a self-interstitial. Both carbon vacancies and interstitials are deep acceptors with localized gap states, and they are both negatively charged in n-type 4H-SiC. Of course, the depth of the resulting FP-related traps will depend on the distance (Coulomb repulsion) between both point defects. This effect is expected to lead to broad and complex DLTS spectra, which is not the case of the M-center.

We also investigated the stability of close pairs of vacancies and interstitials. We found that second neighboring and more remote V_C and C_i defects essentially retain their individual structures and, therefore, show a formation energy of about 10 eV. On the other hand, first neighboring pairs undergo a strong bond reconstruction and energy relaxation. This process is depicted in Fig. 8, where two examples of FP defects are shown. The arrows in Fig. 8(a) help us to understand that the FP(kh) configuration of Fig. 8(b) is obtained upon displacement of the hexagonal C atom (blue) toward the pseudo-cubic site (black) resulting in a fully coordinated C–C dimer next to a V_C defect with a reconstructed Si–Si bond. All remaining atoms retain the "normal" coordination of the SiC crystal (apart from few local bond angle distortions). The result is a rather stable FP whose formation energy is as low as 5.5–6.5 eV in the neutral charge state. Despite their stability, from NEB calculations, we found that the barrier that separates first neighboring FP from annihilation is only 0.1–0.2 eV. Hence, we conclude that such FP defects cannot account for the thermal stability of the M-center.

B. Reconfiguration and migration of the carbon self-interstitial

Due to anisotropy, defects in 4H-SiC migrate differently along the axial and basal directions of the crystal. A prototypical example
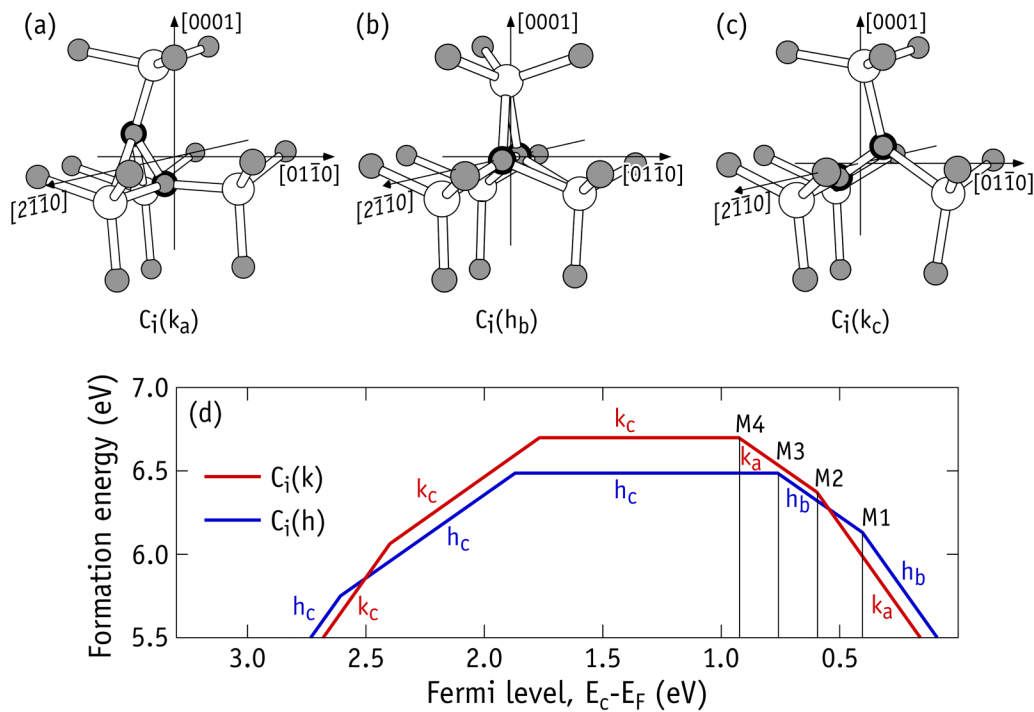
FIG. 7. Atomistic models and calculated formation energy of C_i defects in 4H-SiC. (a) and (b) Structures possessing over-coordinated Si ligands and stable in negative charge states. (c) Under-coordinated C-dimer structures reminiscent of the [001]-split in diamond and stable in the neutral and positive charge states. C and Si atoms are shown in gray and white, respectively. C atoms at the core are highlighted using a thicker line style. (d) Formation energy diagram of C_i defects in 4H-SiC. The red and blue lines denote data concerning C_i states located at cubic (k) and hexagonal (h) sub-lattice sites, respectively.

is the carbon vacancy[59] with measured basal and axial migration barriers of $E_{m,\perp} = 3.7$ eV and $E_{m,\parallel} = 4.2$ eV, respectively.

Basal migration in 4H-SiC involves a single jump between two carbon first neighbors (either k or h neighboring sites). On the
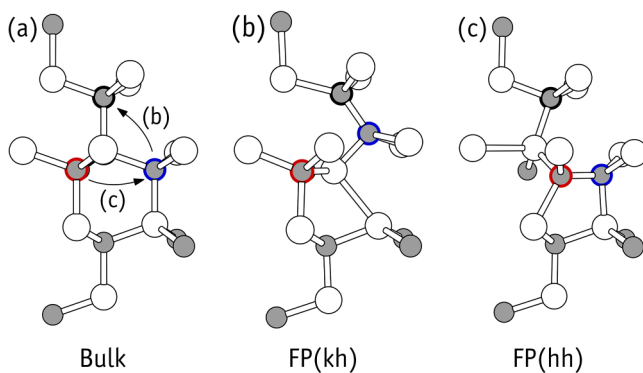

FIG. 8. Atomistic models of first neighboring Frenkel pairs in 4H-SiC. (a) A pristine region of the crystal with arrows indicating the motion of C atoms as to form structures in (b) and (c). Line colors around C atoms are used for the sake of reference and guidance in understanding the formation mechanism.

other hand, a complete axial jump implies traveling at least one [0001] vector of the unit cell, thus spanning both k and h sites. More precisely, axial migration of C_i involves a total of four first neighbor jumps, say $k \rightarrow h \rightarrow k' \rightarrow h' \rightarrow k$. We note that (i) because 4H-SiC is not centrosymmetric, the reverse sequence is not equivalent to the forward sequence, and (ii) the Si first neighbors to the C-dimer atoms in $k \rightarrow h$ (and its symmetrically equivalent $k' \rightarrow h'$) transition show an arrangement identical to that of the basal migration (and to that in 3C-SiC). These geometries differ from $k \rightarrow h'$ (and its symmetrically equivalent $k \rightarrow h'$ jump), where the Si neighbors with respect to C_i change their arrangement in the initial and final states. This feature is depicted in Fig. 9.

Using the NEB method to investigate the minimum energy path for the jumps of C_i in several charge states, we found that $k \leftrightarrow h'$ (and $k' \leftrightarrow h$) barriers are invariably lower than $k \leftrightarrow h$ (and $k' \leftrightarrow h'$) barriers. Barriers for $C_i^=(h_b') \rightarrow C_i^=(k_a)$, $C_i^-(k_a) \rightarrow C_i^-(h_b')$, and $C_i^0(k_a) \rightarrow C_i^0(h_b')$ were estimated as 1.58, 1.22 and 2.10 eV, respectively. Initial and final states of these reconfigurations correspond, respectively, to the most favorable metastable and ground states within each charge state. For the neutral charge state, we assumed the conservation of the $S = 1$ total spin along the jump, and the barrier is markedly higher.[49] The barriers for $C_i^=(h_b') \rightarrow C_i^=(k_a)$ and $C_i^-(k_a) \rightarrow C_i^-(h_b')$ nicely explain the activation energies of 1.4 and 0.9 eV, measured for the kinetics of
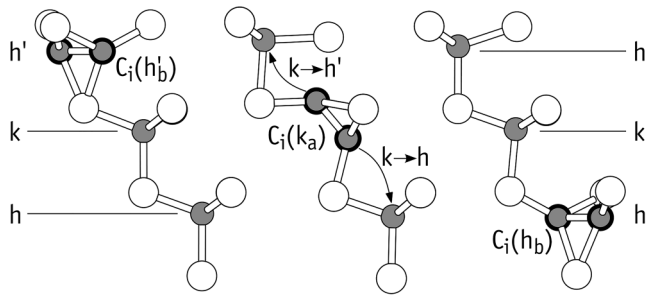
FIG. 9. Atomistic mechanisms for two types of axial jumps of C_i in 4H-SiC. The structure on the left clearly shows that Si neighbors to k and h sites keep their relative locations in the initial and final states of $k \rightarrow h$ jumps. This contrasts with $k \rightarrow h'$ as better perceived on the right-hand structure.

conversion $A \rightarrow B$ and $B \rightarrow A$ upon annealing without bias and under reverse bias, respectively.

While $k \leftrightarrow h'$-type jumps of C_i explain the bistability of the M-center, we argue now that migration is limited by higher energy $k \leftrightarrow h$ barriers. Considering the barriers for jumps starting from the lowest energy configurations for each charge state, we found that $C_i^=(k_a) \rightarrow C_i^=(h_b)$, $C_i^-(h_b) \rightarrow C_i^-(k_a)$, and $C_i^0(h_b) \rightarrow C_i^0(k_a)$ have activation energies of $E_\parallel = 2.10$, 2.20, and 2.73 eV. These are all jumps parallel to the main crystallographic axis. Basal jumps, on the other hand, were found to involve slightly lowers barriers $E_\perp = 1.82$, 1.84, and 2.15 eV.

Considering the doping level of the samples used in Ref. 32 to investigate the annealing behavior of the M-center ($\sim 10^{15}$ cm^{-3}) and that the M-center anneals out in the temperature range of 310–370 °C at a rate of $1.5 \times 10^{13} \exp(-2 \text{ eV}/k_B T)$ s^{-1}, the Fermi level was located at about ~ 0.5 eV below the conduction band bottom, and the M-center was most likely in the negative charge state. The measured activation energy compares well with the calculated barriers for motion of C_i^- along basal and axial directions ($E_\perp = 1.84$ eV eV and $E_\parallel = 2.20$ eV, respectively).

V. DISCUSSION

The M-center forms in irradiated and implanted 4H-SiC irrespectively of the projectile type (2.5-MeV protons,[31] 15-MeV electrons,[32] 7.5-MeV C ions, 2-MeV He ions, fast neutrons,[35] and low energy 200-keV electrons).[33] The above, especially the observation of M in the material irradiated with electrons with energy below the threshold for displacing Si atoms (~ 220 keV),[33] are strong indications that we are dealing with an intrinsic defect on the carbon sublattice.

The charge states of $M_{1/2}$ and M_3 filled traps were inferred, respectively, as double negative and single negative[32] based on the following: (i) No Poole–Frenkel effect was observed for M_1 and M_2, suggesting that they involve the emission of electrons from an acceptor state. (ii) The direct capture cross sections of $M_{1/2}$ and M_3 were about 5×10^{-17} and $> 2 \times 10^{-15}$ cm^2, respectively, suggesting that M_1 and M_2 are emissions from states that are more

repulsive for electrons than M_3. Our measurements and model are consistent with this interpretation.

The existence of a fourth M-peak, corresponding to a $B^- \rightarrow B^0 + e^-$ transition, was indirectly deduced by Nielsen et al.[32] They realized that below 180 K, when either A or B states were filled, they accommodated the same amount of charge. The same was observed above room temperature when both A and B were empty. It was therefore postulated that like spectrum A (M_1 and M_3), configuration B should also possess two electronic transitions (M_2 and an undetected M_4 transition). Although reasonable, this argument lacked hard evidence.

A major limitation of conventional DLTS experiments concerns the fact that it involves a temperature scan. This often poses great difficulty in studying defects with low thermal stability. The reason is that at above a certain temperature, defect transformations and migration may compete with thermal emissions. In the case of the M-center, the M_3 transition ($A^- \rightarrow A^0 + e^-$) is observed at around 300 K, concurrently with $B^- \rightarrow A^-$ conversion. Since the rate of M_4 ($B^- \rightarrow B^0 + e^-$) is expected to be slower than any of the two previous processes, at the temperature at which M_4 is expected to be observed, any B^- state has been already ionized via $B^- \rightarrow A^- \rightarrow A^0 + e^-$, and only M_3 is recorded.

Here, by using isothermal DLTS, we report for the first time a transition involving the M-center, labeled as M4, which is compatible with the "missing" transition of the B state. This transition is also well described by the model.

VI. CONCLUSIONS

An isothermal DLTS study of the M-center in the 2 MeV He ion implanted n-type 4H-SiC material is reported. The newly identified M_4 deep level signal was characterized, along with the M_1, M_2, and M_3 deep levels all arising from the M-center. The M_4 deep level signal and reconfiguration kinetics of the M-center from configuration B to configuration A can result from an electron emission from the M-center in the negative charge state followed by a faster or equally fast reconfiguration in the neutral charge state.

First principles calculations suggest that the M-center in 4H-SiC is a carbon self-interstitial. Besides accounting well for the observed character and location of levels M_1–M_4, nudged elastic band calculations lead to energy barriers for reconfiguration and migration that are very close to the activation barriers measured for cycling between $A \leftrightarrow B$ spectra and for the annealing of the M-center. We also provide calculations and arguments against a connection between the M-center and a carbon Frenkel pair.

DATA AVAILABLITY

The data that support the findings of this study are available from the corresponding author upon reasonable request.

REFERENCES

[1]T. Kimoto and J. A. Cooper, *Fundamentals of Silicon Carbide Technology* (John Wiley & Sons Singapore Pte. Ltd, Singapore, 2014).

[2]X. She, A. Q. Huang, O. Lucia, and B. Ozpineci, IEEE Trans. Ind. Electron. **64**, 8193 (2017).

[3]L. Liu, A. Liu, S. Bai, L. Lv, P. Jin, and X. Ouyang, Sci. Rep. **7**, 13376 (2017).

[4]F. Franceschini and F. H. Ruddy, *Properties and Applications of Silicon Carbide* (InTech, 2011).

[5]J. Coutinho, V. J. B. Torres, I. Capan, T. Brodar, Z. Ereš, R. Bernat, V. Radulović, K. Ambrožič, L. Snoj, Ž Pastuović, A. Sarbutt, T. Ohshima, Y. Yamazaki, and T. Makino, Nucl. Instrum. Methods Phys. Res. Sect. A **986**, 164793 (2021).

[6]J. R. Weber, W. F. Koehl, J. B. Varley, A. Janotti, B. B. Buckley, C. G. Van de Walle, and D. D. Awschalom, Proc. Natl. Acad. Sci. U.S.A. **107**, 8513 (2010).

[7]W. F. Koehl, B. B. Buckley, F. J. Heremans, G. Calusine, and D. D. Awschalom, Nature **479**, 84 (2011).

[8]V. Ivády, J. Davidsson, N. Delegan, A. L. Falk, P. V. Klimov, S. J. Whiteley, S. O. Hruszkewycz, M. V. Holt, F. J. Heremans, N. T. Son, D. D. Awschalom, I. A. Abrikosov, and A. Gali, Nat. Commun. **10**, 5607 (2019).

[9]S. Castelletto and A. Boretti, J. Phys. Photonics **2**, 022001 (2020).

[10]N. T. Son, X. T. Trinh, L. S. Løvlie, B. G. Svensson, K. Kawahara, J. Suda, T. Kimoto, T. Umeda, J. Isoya, T. Makino, T. Ohshima, and E. Janzén, Phys. Rev. Lett. **109**, 187603 (2012).

[11]N. T. Son, P. Stenberg, V. Jokubavicius, T. Ohshima, J. Ul Hassan, and I. G. Ivanov, J. Phys.: Condens. Matter **31**, 195501 (2019).

[12]C. G. Hemmingsson, N. T. Son, A. Ellison, J. Zhang, and E. Janzén, Phys. Rev. B **58**, R10119 (1998).

[13]I. Capan, T. Brodar, Z. Pastuović, R. Siegele, T. Ohshima, S. I. Sato, T. Makino, L. Snoj, V. Radulović, J. Coutinho, V. J. B. Torres, and K. Demmouche, J. Appl. Phys. **123**, 161597 (2018).

[14]I. Capan, T. Brodar, J. Coutinho, T. Ohshima, V. P. Markevich, and A. R. Peaker, J. Appl. Phys. **124**, 245701 (2018).

[15]M. E. Bathen, A. Galeckas, J. Müting, H. M. Ayedh, U. Grossner, J. Coutinho, Y. K. Frodason, and L. Vines, NPJ Quantum Inf. **5**, 111 (2019).

[16]M. Wagner, B. Magnusson, W. M. Chen, E. Janzén, E. Sörman, C. Hallin, and J. L. Lindström, Phys. Rev. B **62**, 16555 (2000).

[17]E. Janzén, A. Gali, P. Carlsson, A. Gällström, B. Magnusson, and N. T. Son, Phys. B: Condens. Matter **404**, 4354 (2009).

[18]X. T. Trinh, K. Szász, T. Hornos, K. Kawahara, J. Suda, T. Kimoto, A. Gali, E. Janzén, and N. T. Son, Phys. Rev. B **88**, 235209 (2013).

[19]J. Coutinho, V. J. B. Torres, K. Demmouche, and S. Öberg, Phys. Rev. B **96**, 174105 (2017).

[20]R. Kuate Defo, X. Zhang, D. Bracher, G. Kim, E. Hu, and E. Kaxiras, Phys. Rev. B **98**, 104103 (2018).

[21]P. Udvarhelyi, G. Thiering, N. Morioka, C. Babin, F. Kaiser, D. Lukin, T. Ohshima, J. Ul-Hassan, N. T. Son, J. Vučković, J. Wrachtrup, and A. Gali, Phys. Rev. Appl. **13**, 054017 (2020).

[22]V. Ivády, J. Davidsson, N. T. Son, T. Ohshima, I. A. Abrikosov, and A. Gali, Phys. Rev. B **96**, 161114 (2017).

[23]T. Kimoto, A. Itoh, H. Matsunami, S. Sridhara, L. L. Clemen, R. P. Devaty, W. J. Choyke, T. Dalibor, C. Peppermüller, and G. Pensl, Appl. Phys. Lett. **67**, 2833 (1995).

[24]C. Hemmingsson, N. T. Son, O. Kordina, J. P. Bergman, E. Janzén, J. L. Lindström, S. Savage, and N. Nordell, J. Appl. Phys. **81**, 6155 (1997).

[25]T. Hiyoshi and T. Kimoto, Appl. Phys. Express **2**, 041101 (2009).

[26]L. S. Løvlie and B. G. Svensson, Appl. Phys. Lett. **98**, 052108 (2011).

[27]N. T. Son, P. N. Hai, and E. Janzén, Mater. Sci. Forum **353–356**, 499 (2001).

[28]T. T. Petrenko, T. L. Petrenko, and V. Y. Bratus, J. Phys.: Condens. Matter **14**, 12433 (2002).

[29]A. Gali, P. Deák, E. Rauls, N. T. Son, I. G. Ivanov, F. H. C. Carlsson, E. Janzén, and W. J. Choyke, Phys. B: Condens. Matter **340–342**, 175 (2003).

[30]M. Bockstedte, M. Heid, and O. Pankratov, Phys. Rev. B **67**, 193102 (2003).

[31]D. M. Martin, H. Kortegaard Nielsen, P. Lévêque, A. Hallén, G. Alfieri, and B. G. Svensson, Appl. Phys. Lett. **84**, 1704 (2004).

[32]H. K. Nielsen, A. Hallén, and B. G. Svensson, Phys. Rev. B **72**, 085208 (2005).

[33]F. C. Beyer, C. Hemmingsson, H. Pedersen, A. Henry, E. Janzén, J. Isoya, N. Morishita, and T. Ohshima, J. Appl. Phys. **109**, 103703 (2011).

[34]G. Alfieri and A. Mihaila, J. Phys.: Condens. Matter **32**, 465703 (2020).

[35]T. Brodar, L. Bakrač, I. Capan, T. Ohshima, L. Snoj, V. Radulović, and Ž Pastuović, Crystals **10**, 845 (2020).

[36]A. Gali, P. Deák, P. Ordejón, T. Son, E. Janzén, and J. Choyke, Phys. Rev. B **68**, 125201 (2003).

[37]M. Bockstedte, A. Mattausch, and O. Pankratov, Phys. Rev. B **68**, 205201 (2003).

[38]G. Alfieri, E. V. Monakhov, B. G. Svensson, and M. K. Linnarsson, J. Appl. Phys. **98**, 043518 (2005).

[39]M. L. David, G. Alfieri, E. M. Monakhov, A. Hallén, C. Blanchard, B. G. Svensson, and J. F. Barbot, J. Appl. Phys. **95**, 4728 (2004).

[40]H. M. Ayedh, V. Bobal, R. Nipoti, A. Hallén, and B. G. Svensson, J. Appl. Phys. **115**, 012005 (2014).

[41]L. Storasta, J. P. Bergman, E. Janzén, A. Henry, and J. Lu, J. Appl. Phys. **96**, 4909 (2004).

[42]R. Karsthof, M. E. Bathen, A. Galeckas, and L. Vines, Phys. Rev. B **102**, 184111 (2020).

[43]T. Umeda, N. T. Son, J. Isoya, E. Janzén, T. Ohshima, N. Morishita, H. Itoh, A. Gali, and M. Bockstedte, Phys. Rev. Lett. **96**, 145501 (2006).

[44]J. W. Steeds, Phys. Rev. B **80**, 245202 (2009).

[45]N. T. Son, P. Stenberg, V. Jokubavicius, H. Abe, T. Ohshima, J. Ul Hassan, and I. G. Ivanov, Appl. Phys. Lett. **114**, 212105 (2019).

[46]K. Szász, V. Ivády, I. A. Abrikosov, E. Janzén, M. Bockstedte, and A. Gali, Phys. Rev. B **91**, 121201 (2015).

[47]J. Coutinho, Crystals **11**, 167 (2021).

[48]A. Gali, Mater. Sci. Forum **679–680**, 225 (2011).

[49]J. Coutinho, J. D. Gouveia, T. Makino, T. Ohshima, Ž. Pastuović, L. Bakrač, T. Brodar, and I. Capan, Phys. Rev. B **103**, L180102 (2021).

[50]M. Ito, L. Storasta, and H. Tsuchida, Appl. Phys. Express **1**, 015001 (2008).

[51]Ž. Pastuović, R. Siegele, I. Capan, T. Brodar, S. Sato, and T. Ohshima, J. Phys.: Condens. Matter **29**, 475701 (2017).

[52]Y. Tokuda, J. Appl. Phys. **100**, 023704 (2006).

[53]G. Kresse and J. Furthmüller, Comput. Mater. Sci. **6**, 15 (1996).

[54]J. Heyd, G. E. Scuseria, and M. Ernzerhof, J. Chem. Phys. **118**, 8207 (2003).

[55]J. Heyd, G. E. Scuseria, and M. Ernzerhof, J. Chem. Phys. **124**, 219906 (2006).

[56]P. E. Blöchl, Phys. Rev. B **50**, 17953 (1994).

[57]G. Kresse and D. Joubert, Phys. Rev. B **59**, 1758 (1999).

[58]J. P. Perdew, K. Burke, and M. Ernzerhof, Phys. Rev. Lett. **77**, 3865 (1996).

[59]M. E. Bathen, J. Coutinho, H. M. Ayedh, J. Ul Hassan, I. Farkas, S. Öberg, Y. K. Frodason, B. G. Svensson, and L. Vines, Phys. Rev. B **100**, 014103 (2019).

[60]C. Freysoldt, J. Neugebauer, and C. G. Van de Walle, Phys. Rev. Lett. **102**, 016402 (2009).

[61]G. Henkelman, B. P. Uberuaga, and H. Jónsson, J. Chem. Phys. **113**, 9901 (2000).

[62]Y. Tokuda, N. Shimizu, and A. Usami, Jpn. J. Appl. Phys. **18**, 309 (1979).

[63]Y. Zohta and M. O. Watanabe, J. Appl. Phys. **53**, 1809 (1982).

[64]D. Pons, J. Appl. Phys. **55**, 3644 (1984).

[65]D. C. Hunt, D. J. Twitchen, M. E. Newton, J. M. Baker, T. R. Anthony, W. F. Banholzer, and S. S. Vagarali, Phys. Rev. B **61**, 3863 (2000).